# Supporting Information

# Interface Coordination Nucleation of Copper Nanoclusters on Covalent Organic Frameworks for Electrocatalytic Ammonia Synthesis

**Authors:**

Minghang Jiang,[a,b,c,#,*] Fasheng Chen,[a,c,#] Xinyu Zhong,[d,#] Huaizhu Wang,[b] Junjie Ding,[e] Xuemei Liao,[a,c] Zhenju Jiang,[a,c] Xiaojun Luo,[a] Lei Li,[a,*] Yan Xiong,[b,*] and Zhong Jin,[b,*]

**Affiliations:**

[a] Department of Chemistry, School of Science, Xihua University, Chengdu, Sichuan 610039, P. R. China.

[b] State Key Laboratory of Coordination Chemistry, MOE Key Laboratory of Mesoscopic Chemistry, MOE Key Laboratory of High Performance Polymer Materials and Technology, Jiangsu Key Laboratory of Clean Energy Catalysis and Intelligent Green Chemical Engineering, Suzhou Key Laboratory of Green Intelligent Manufacturing of New Energy Materials and Devices, Tianchang New Materials and Energy Technologies Research Center, Institute of Green Chemistry and Engineering, School of Chemistry and Chemical Engineering, Nanjing University, Nanjing, Jiangsu 210023, P. R. China.

[c] School of Food and Biological Engineering, Xihua University, Chengdu, Sichuan 610039, P. R. China.

[d] College of Nuclear Technology and Automation Engineering, Chengdu University of Technology, Chengdu 610059, P. R. China.

[e] College of Physics and Center of Quantum Materials and Devices, Chongqing University, Chongqing 401331, P. R. China.

[#] These authors contributed equally to this work.

* Address correspondence to minghang@mail.xhu.edu.cn; leili@xhu.edu.cn; xiongyan@nju.edu.cn; zhongjin@nju.edu.cn

## EXPERIMENTAL SECTION

### Material characterizations

The surface morphology and structure of the material were investigated by scanning electron microscopy (SEM, YB-200E) and transmission electron microscopy (TEM, JEM-2100F). SEM and elemental mapping images tests were carried out on a Talos F200i instrument. Powder X-ray diffraction (XRD) analysis was carried out by a Bruker D-8 Advance diffractometer with a Cu *Kα* X-ray source from 2 and 35° with a scanning rate of 2° $min^{-1}$. The surface element compositions and detailed valence states of all catalysts were probed by X-ray photoelectron spectroscopy (XPS) via a PHI-5000 Versa Probe instrument. The samples underwent analysis via Fourier transform infrared spectroscopy (FTIR, Nicolet IS10). The UV–Vis absorbance spectra were measured on a UV-2700 instrument. The nitrogen adsorption and desorption isotherms were measured at 77 K using a Micromeritics ASAP 2020M system. The samples were outgassed at 80 °C for 2 h before the measurements. The Brunauer Emmett Teller (BET) method was used to calculate the surface area from the adsorption data. The pore-size-distribution curves were obtained via the nonlocal density functional theory (NLDFT) method.

### Extended X-ray absorption fine structure (EXAFS) and X-ray absorption fine structure (XAFS) analyses

Data reduction, data analysis, and EXAFS fitting were performed and analyzed with the Athena and Artemis programs of the Demeter data analysis packages that utilizes the FEFF6 program to fit the EXAFS data. The energy calibration of the sample was conducted through standard Cu foil, which as a reference and was simultaneously measured. A linear function was subtracted from the pre-edge region, then the edge jump was normalized using Athena software. The χ(k) data were isolated by subtracting a smooth, third-order polynomial approximating the absorption background of an isolated atom. The $k^3$-weighted $\chi(k)$ data were Fourier transformed

after applying a HanFeng window function ($\Delta k$ = 1.0). For EXAFS modeling, the global amplitude EXAFS (*CN, R,* $\sigma^2$ and $\Delta E_0$) were obtained by nonlinear fitting, with least-squares refinement, of the EXAFS equation to the Fourier-transformed data in *R*-space, using Artemis software, EXAFS of the Cu foil are fitted and the obtained amplitude reduction factor $S_0^2$ value (1) was set in the EXAFS analysis to determine the coordination numbers (*CNs*) in the Cu-Cu scattering path in sample.

**Determination of ammonia**

The concentration of ammonia product was spectrophotometrically detected by the standard indophenol blue indicator method. Briefly, 2 mL of the solution product, 2 mL of a 1 M NaOH solution with 5% salicylic acid and 5% sodium citrate, 1 mL of 0.05 M NaClO and 0.2 mL of 1% sodium nitroferricyanide (III) dihydrate ($C_5FeN_6Na_2O{\cdot}2H_2O$) solution were mixed. After standing in the dark for 2 h, the concentration of indophenol blue was detected by ultraviolet-visible (UV-*vis*) spectrophotometer at a wavelength of 655 nm in the absorption spectrum.

**Determination of $NO_2^-$**

5.0 mL of a 1 g/L solution of N-(1-naphthyl) ethylenediamine dihydrochloride, along with 5.0 mL of glacial acetic acid, are introduced into a volumetric flask. Subsequently, the solution is made up to a total volume of 100 milliliters with a 5 g/L sulfanilamide solution to form a uniform solution and used as the chromogenic reagent. Then, 1.0 mL of electrolyte was collected from the cathode compartment and mixed with 4.0 mL of chromogenic reagent. After standing for 20 min in the dark for at room temperature, the light absorbance of the resulting solution was detected by an UV-*vis* absorption spectrophotometer at a wavelength of 540 nm in the absorption spectrum.

**Determination of hydrazine**

The possible $N_2H_4$ product in the electrolyte solution was measured by the Watt-Chrisp method. Briefly, 10 mL of HCl, 2 g of para-(dimethylamino) benzaldehyde and 100 mL of $C_2H_5OH$ were dissolved and used as a sensitive chromogenic reagent. Then, 2 mL of solution product was collected from the cathode compartment and uniform mixed with 5 mL of the chromogenic reagent at room temperature. After standing for 20 min in the dark for at room temperature, the light absorbance of the solution was detected by UV-*vis* spectrophotometer at the wavelength of 457 nm.

**$^{15}$N-Isotope labelling experiments**

In the case of NITRR, the isotope labelling experiment was carried out to clarify the source of ammonia by using $^{15}KNO_3$ (98 atom % $^{15}N$) as the raw material. After the NITRR test for 1 h at -1.0 V (vs. RHE) in 0.1 mM $Na_2SO_4$ solution, 10 mL of electrolyte was collected from the cathode chamber. To prepare the NMR sample, 0.6 mL of the liquid product and acidified with 0.1 mL of 1 M $H_2SO_4$ solution. Then, 550 μL of the above mixture was put into a NMR tube, and $D_2O$ was added to a closed tube with a higher height of liquid level as a calibration sample for $^1H$ NMR analysis. The one dimensional $^1H$ NMR spectra were collected by a superconducting Fourier transform NMR spectrometer (Bruker Avance-400) with the necessary suppression of water peaks by a water pre-saturation method.

**Computational methods**

The spin-polarized first-principles calculations based on the Density Functional Theory (DFT) were performed using the Vienna Ab initio Simulation Package (VASP)[S1-S3]. The Perdew-Burke-Ernzerhof (PBE) exchange-correlation functional[S4] within the generalized gradient approximation (GGA) was employed to describe the exchange-correlation energy. The projector-augmented-wave (PAW)[S5] method was adopted for the pseudopotentials. The energy cutoff for the plane wave basis

expansion was set to 450 eV. The force on each atom was set as 0.02 eV/Å for convergence criterion. Slab model of 0.5-Cu NCs/HL-COF was constructed in a 1×1×1 supercell, with a vacuum layer of 15 Å in the z direction to avoid the interaction between layers, where the $CuO_x$ part was constructed with a $Cu_{12}O_{12}$ atomic cluster. The sampling in the Brillouin zone was set with a single gamma point[S6]. The van der Waals interaction was considered by using DFT-D3 method. The (111) surface of pure CuO was also constructed and calculated as a comparison. The free energies of the NITRR were calculated by the equation[S7]: $\Delta G=\Delta E_{DFT}+\Delta E_{ZPE}-T\Delta S$, where $\Delta E_{DFT}$ is the DFT electronic energy difference of each step, $\Delta E_{ZPE}$ and $\Delta S$ are the correction of zero-point energy and the variation of entropy, respectively, which are obtained by vibration calculations, T is the temperature (T = 300 K). The concrete data for zero-point energy and the variation of entropy are listed in Table S3.

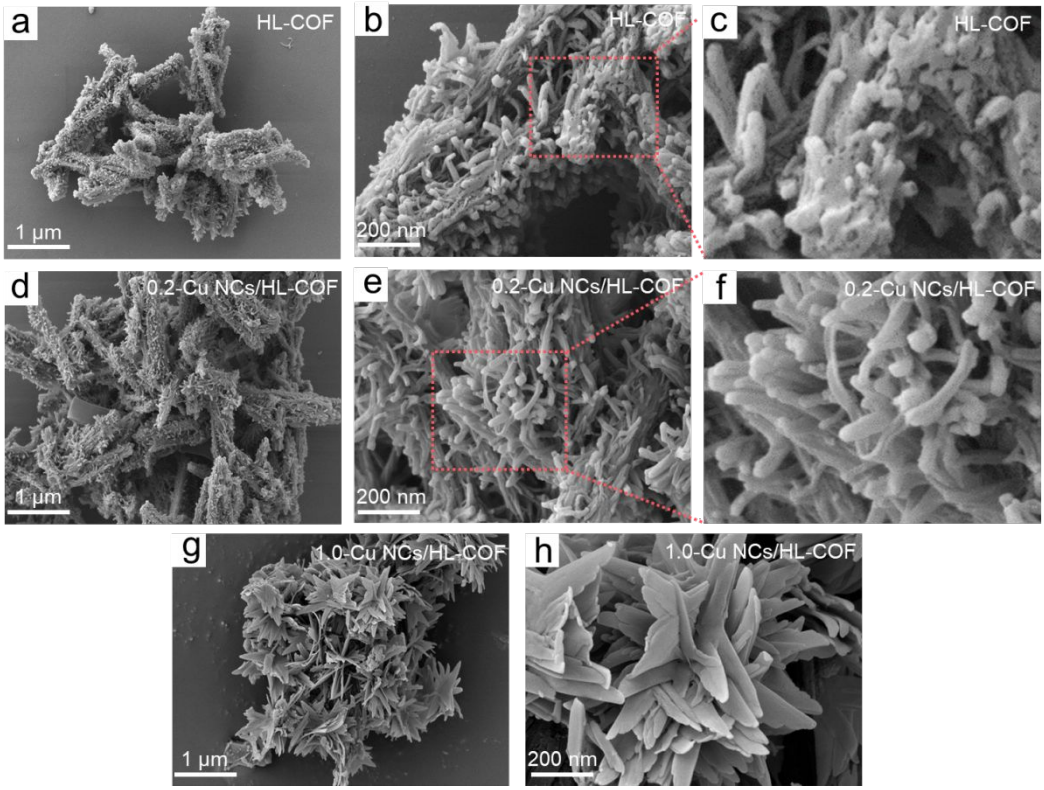


**Figure S1.** SEM images of (a-c) HL-COF, (d-f) 0.2-Cu NCs/HL-COF, and (g-h) 1.0-Cu NCs/HL-COF samples.

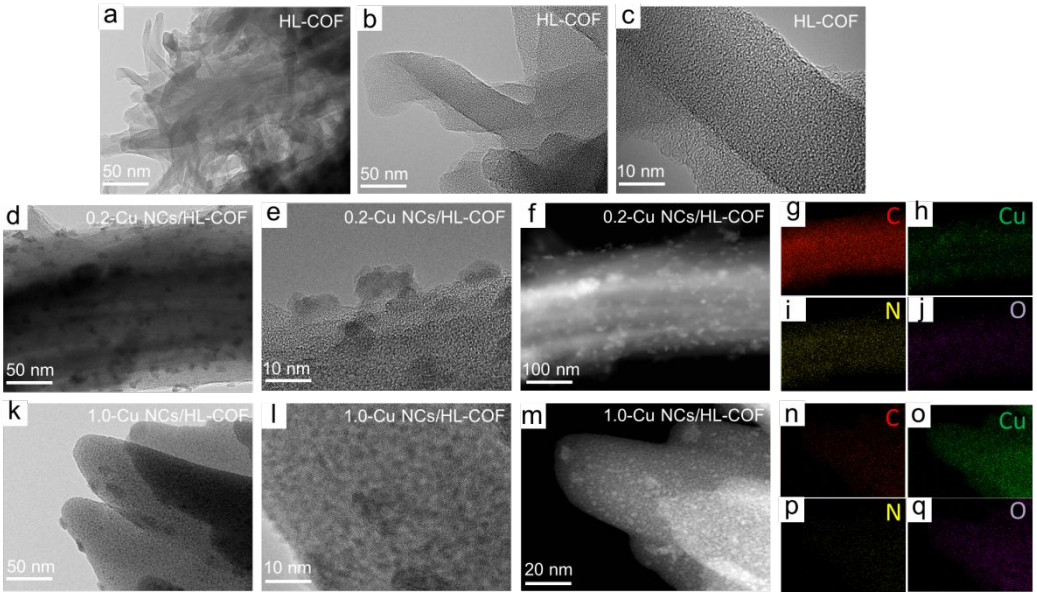


**Figure S2.** (a-c) TEM images of HL-COF and (d-e) 0.2-Cu NCs/HL-COF samples. (f-j) elemental mapping images of 0.2-Cu NCs/HL-COF sample. (k-l) TEM and (m-q) elemental mapping images of 1.0-Cu NCs/HL-COF sample.

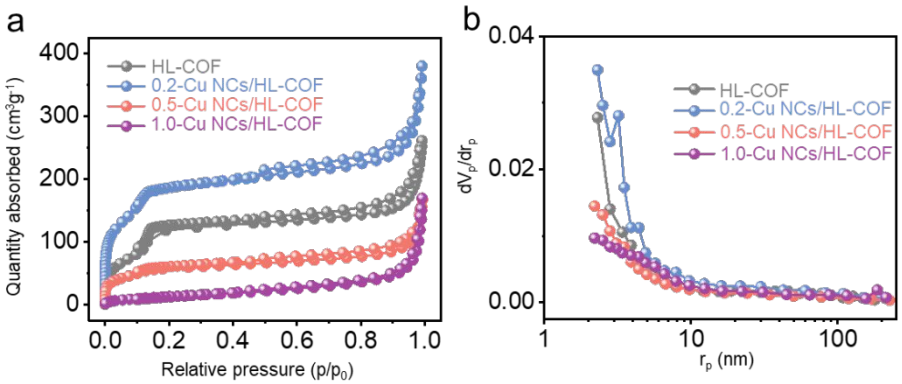


**Figure S3.** (a) Nitrogen adsorption isotherms and (b) pore size distribution plots of HL-COF, 0.2-Cu NCs/HL-COF, 0.5-Cu NCs/HL-COF, and 1.0-Cu NCs/HL-COF samples.

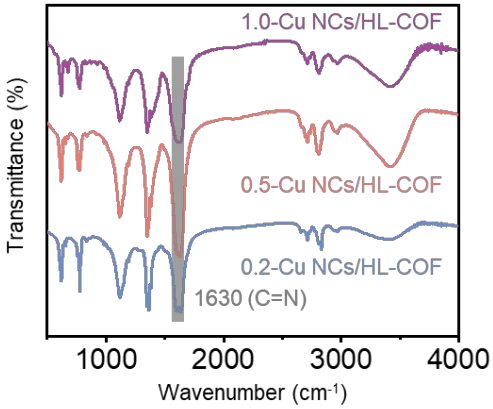


146

147 **Figure S4.** FTIR spectra of 0.2-Cu NCs/HL-COF, 0.5-Cu NCs/HL-COF, and 1.0-Cu

148 NCs/HL-COF samples.

149

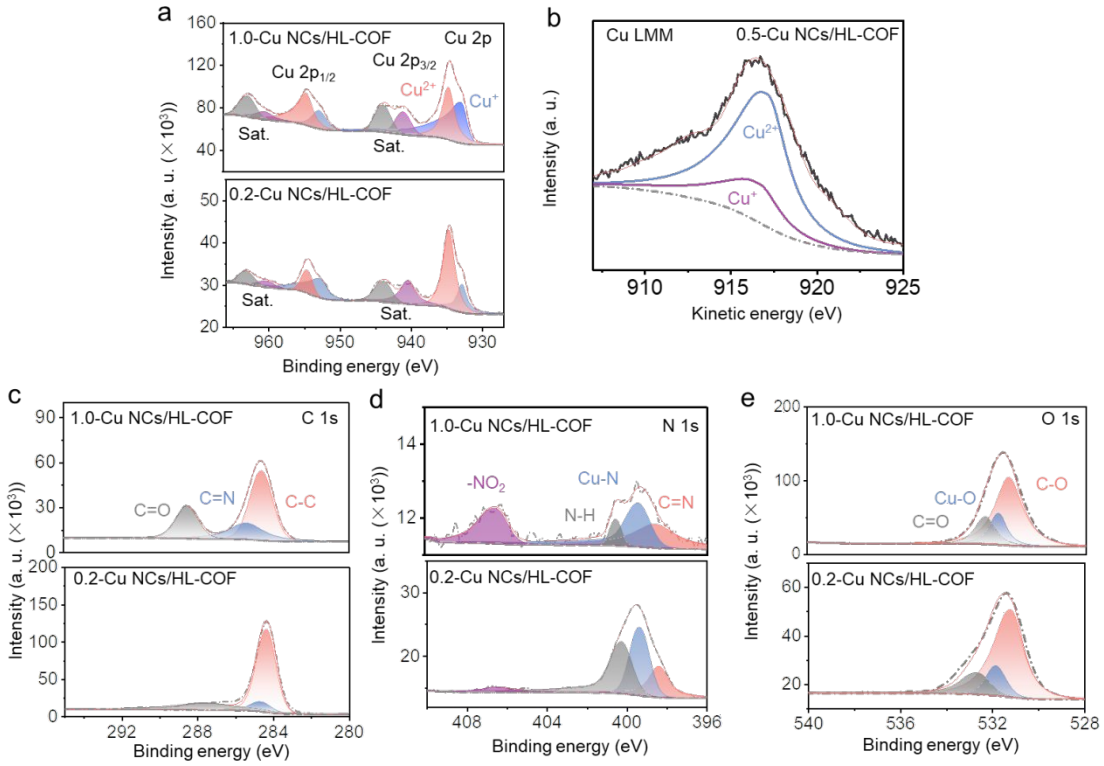


150

151 **Figure S5.** High-resolution XPS spectra at the (a) Cu2p regions of 0.2-Cu
152 NCs/HL-COF, and 1.0-Cu NCs/HL-COF samples. (b) Cu LMM AES spectra of
153 0.5-Cu NCs/HL-COF. High-resolution XPS spectra at (c) C1s, (d) N1s and (e) O1s
154 regions of 0.2-Cu NCs/HL-COF, and 1.0-Cu NCs/HL-COF samples.

155

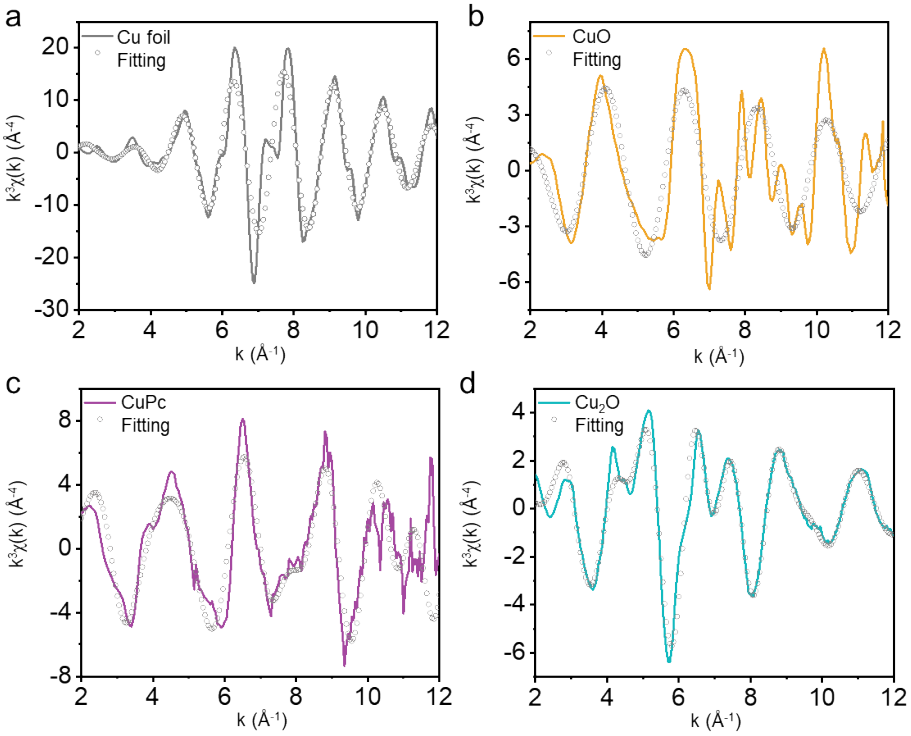


156

157 **Figure S6.** The fitting result of the EXAFS spectrum for the Cu element of single (a)

158 Cu foil, (b) CuO, (c) CuPc, and (d) $Cu_2O$ samples at k-space.

159

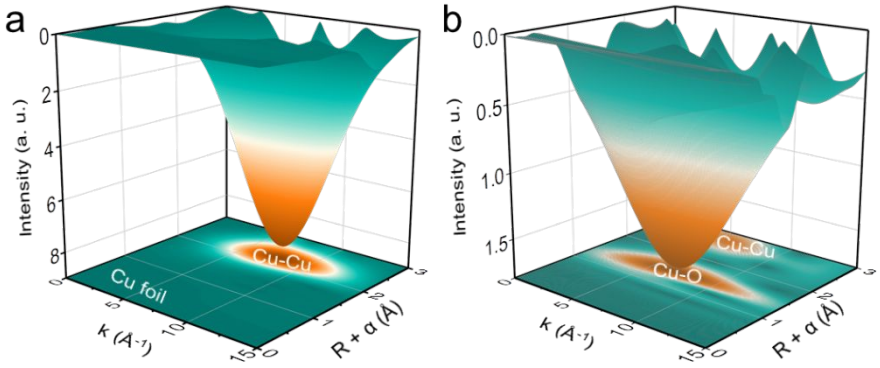


160

161 **Figure S7.** WT of the Cu K-edge FT-EXAFS spectra of (a) Cu foil and (b) $Cu_2O$

162 samples.

163

164

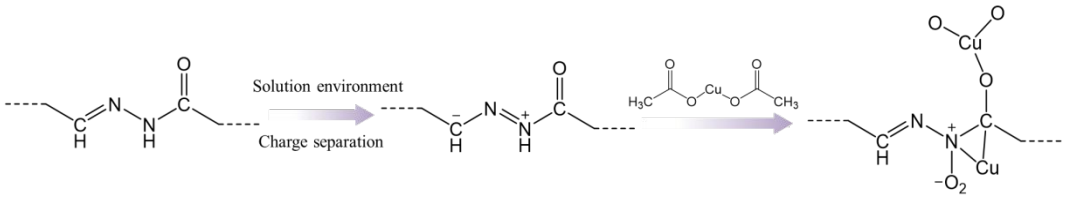


**Figure S8.** Possible interface coordination nucleation mechanism of copper nanoclusters within the HL-COF structure.

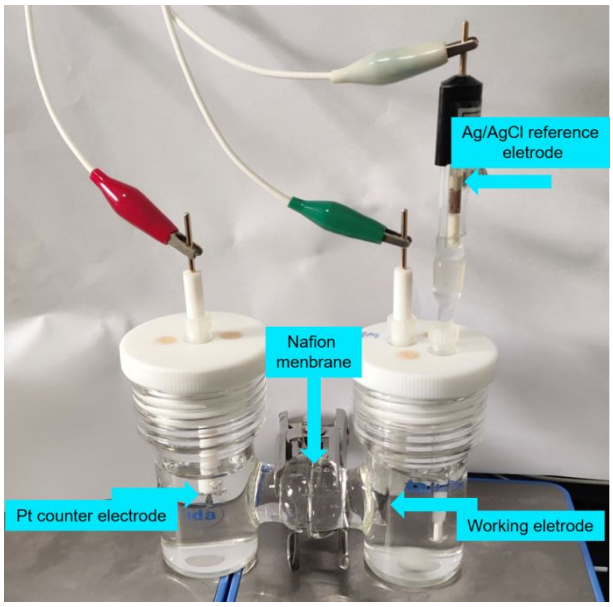


**Figure S9.** Optical photograph of NITRR reactor with two compartments separated by a Nafion-117 proton exchange membrane.

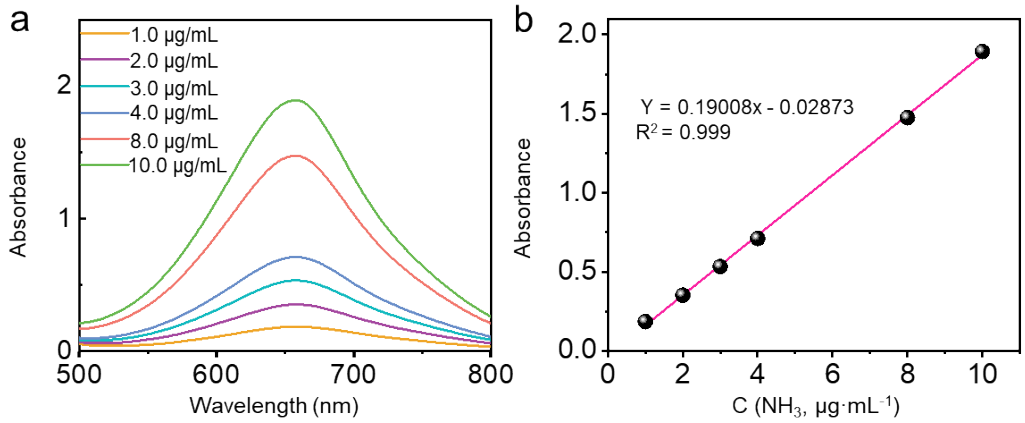


**Figure S10**. (a) UV-*vis* absorption spectrum of ammonia standard solution with different concentrations and coloured with indophenol indicator. (b) Linear relationship between the light absorbance at 655 nm wavelength measured by UV-*vis* spectrophotometer and the concentration of ammonia standard solution.

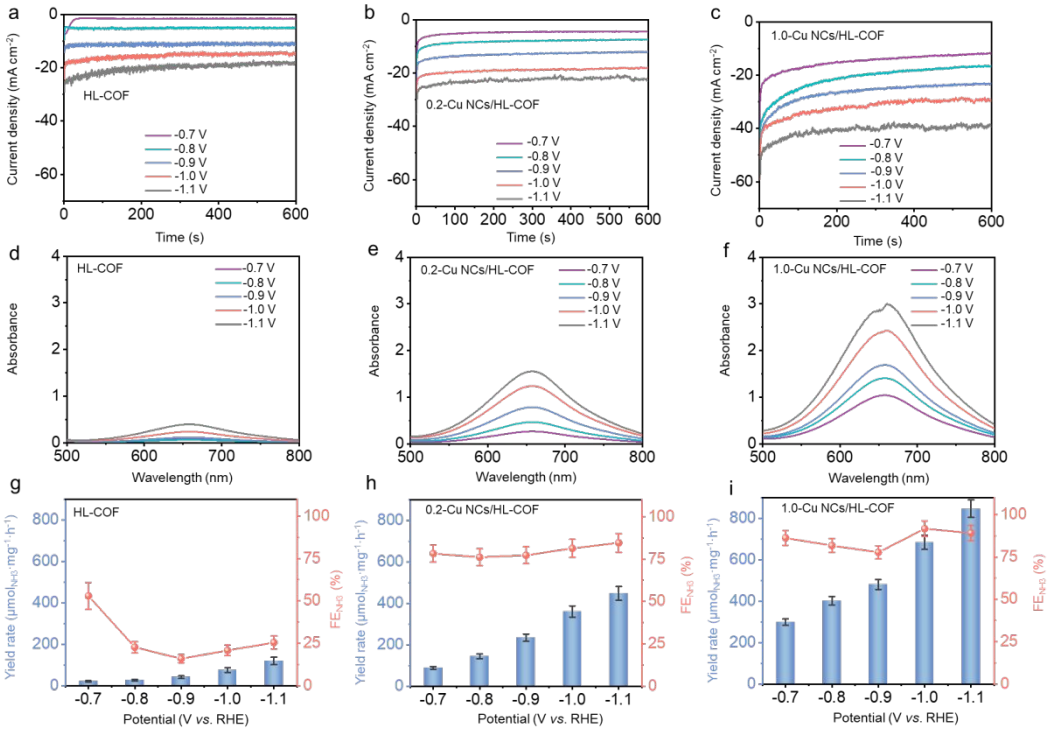


**Figure S11.** Time-dependent current density curves of (a) HL-COF, (b) 0.2-Cu NCs/HL-COF and (c) 1.0-Cu NCs/HL-COF samples under different applied potentials for the NITRR. UV-*vis* absorption spectra of the electrolytes after the NITRR test for 10 min of the (d) HL-COF, (e) 0.2-Cu NCs/HL-COF and (f) 1.0-Cu NCs/HL-COF samples at different potentials and colored with indophenol indicator. The $NH_3$ yield and corresponding $FE_{NH3}$ of the (g) HL-COF, (h) 0.2-Cu NCs/HL-COF and (i) 1.0-Cu NCs/HL-COF samples at different applied potentials for the NITRR (Error bars are made using the standard deviation of three experiment repeats).

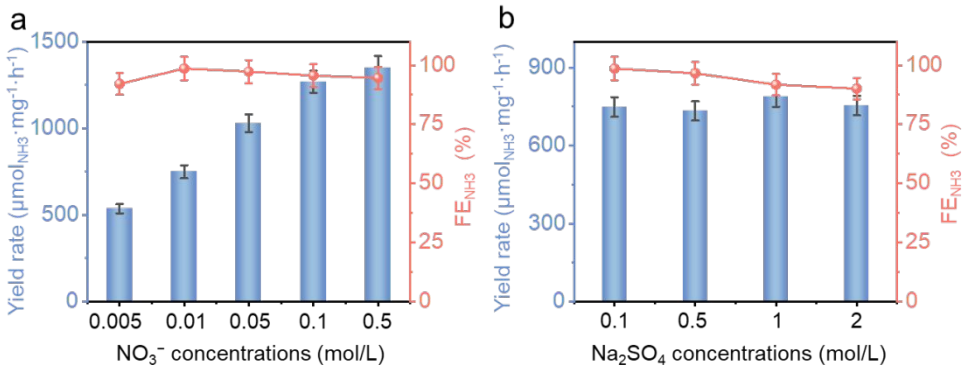


**Figure S12.** (a) The $NH_3$ yield and corresponding $FE_{NH3}$ of 0.5-Cu NCs/HL-COF at -1.0 V vs. RHE in a 0.1 M $Na_2SO_4$ solution containing varying concentrations of $KNO_3$ for electrochemical NITRR (Error bars are made using the standard deviation of three experiment repeats). (b) The $NH_3$ yield and corresponding $FE_{NH3}$ of 0.5-Cu NCs/HL-COF at -1.0 V vs. RHE in a 0.01M $KNO_3$ containing varying concentrations of $Na_2SO_4$ for electrochemical NITRR (Error bars are made using the standard deviation of three experiment repeats).

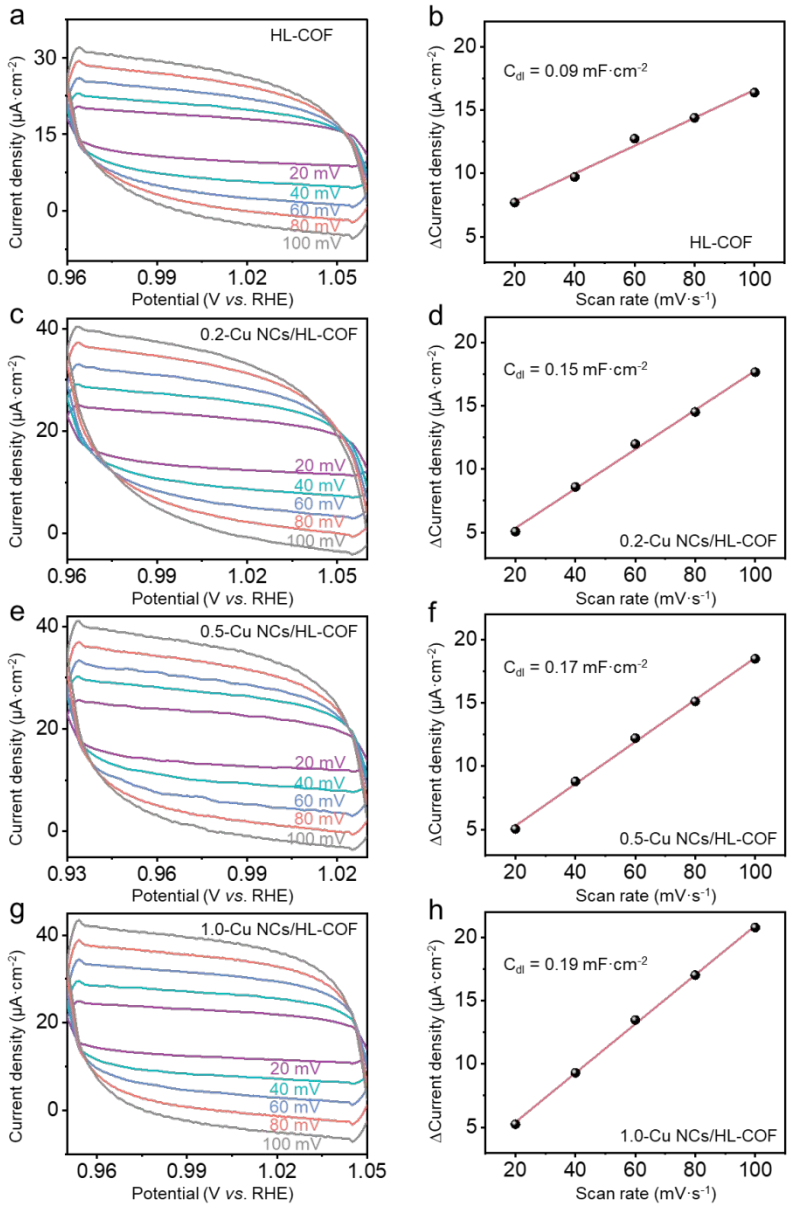


**Figure S13.** (a, c, e, and g) CV curves measured at different scan rates and (b, d, f, and h) corresponding double-layer capacitances ($C_{dl}$) plots of (a, b) HL-COF, (c, d) 0.2-Cu NCs/HL-COF, (e, f) 0.5-Cu NCs/HL-COF, (g, h) 1.0-Cu NCs/HL-COF, respectively.

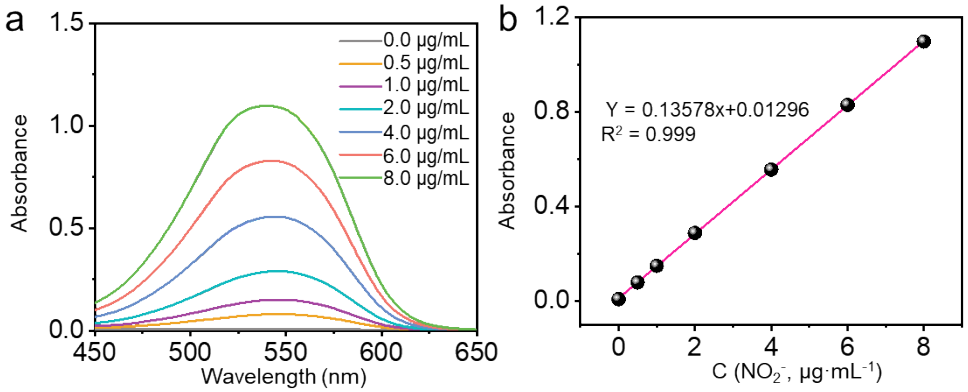


205

206 **Figure S14.** (a) UV-*vis* absorption spectra of the $NO_2^-$ standard solution with
207 different concentrations and coloured with the spectrophotometric method employing
208 N-(1-Naphthyl)-ethylenediamine dihydrochloride indicator. (b) Linear relationship
209 between the light absorbance at 540 nm wavelength measured by UV-*vis*
210 spectrophotometer and the concentration of $NO_2^-$ standard solution.

211

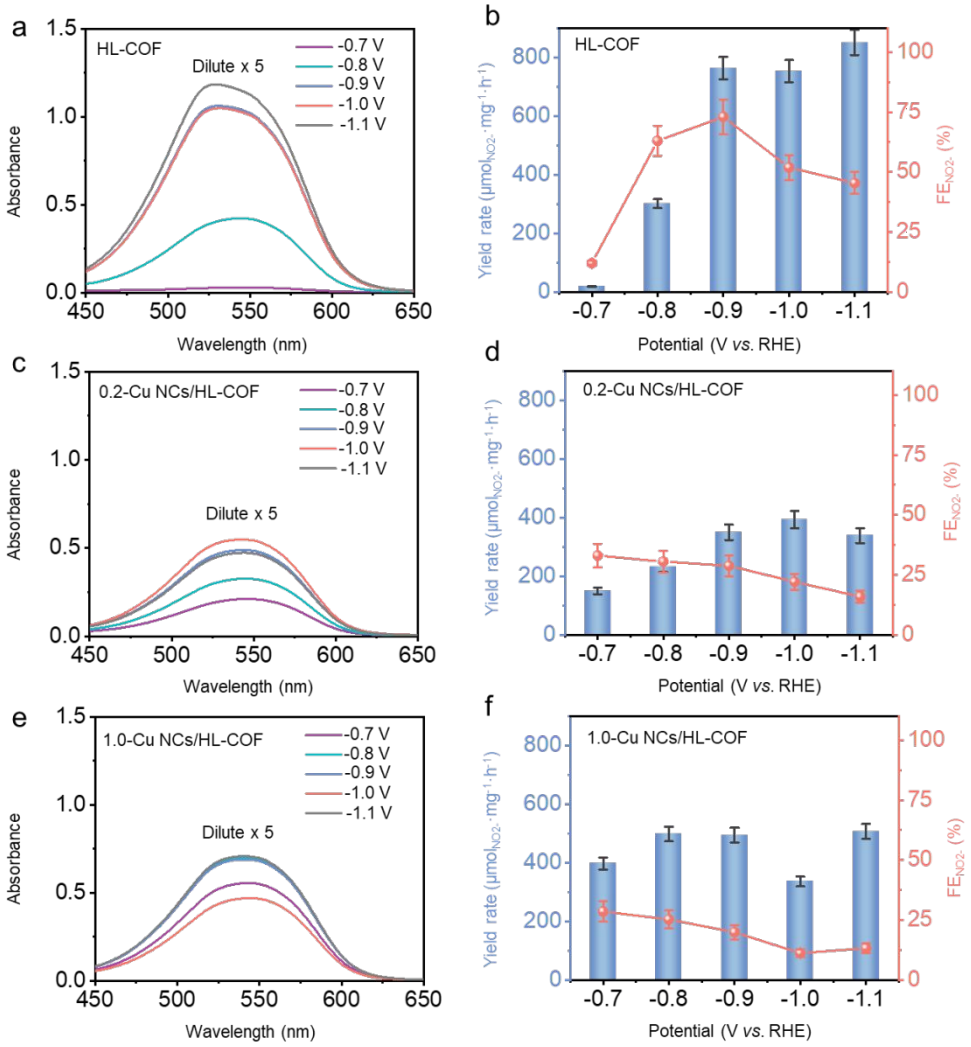


**Figure S15.** UV-*vis* absorption spectra of the electrolyte solution after the NITRR test of (a) HL-COF, (c) 0.2-Cu NCs/HL-COF and (e) 1.0-Cu NCs/HL-COF samples at various applied potentials and then coloured by the Griess indicator. The $NO_2^-$ yield and corresponding $FE_{NO2-}$ of the (b) HL-COF, (d) 0.2-Cu NCs/HL-COF and (f) 1.0-Cu NCs/HL-COF samples at different applied potentials for the NITRR (Error bars are made using the standard deviation of three experiment repeats).

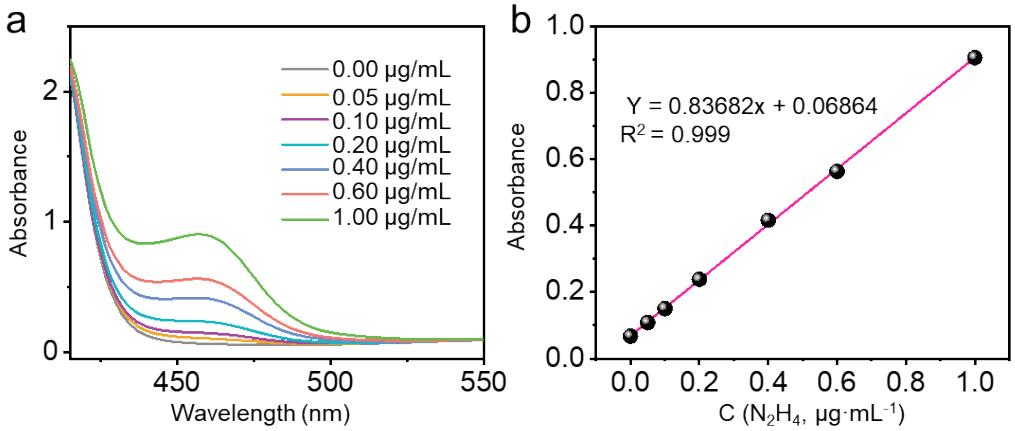


220

221 **Figure S16.** (a) UV-*vis* absorption spectra of standard $N_2H_4$ solutions with various

222 concentrations and coloured by para-dimethylamino-benzaldehyde indicator. (b)

223 Linear relationship between the light absorbance at 457 nm wavelength measured by

224 UV-*vis* spectrophotometer and the concentration of $N_2H_4$ standard solution.

225

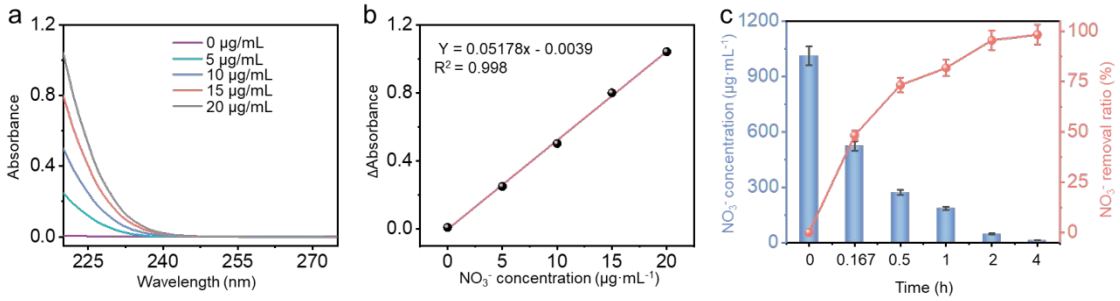


**Figure S17**. (a) UV-vis absorption spectra of standard $NO_3^-$ solution with various concentrations colored by sulfamic acid indicator. (b) Calibration curve used for the calculation of $NO_3^-$ concentrations. ΔA is defined as the difference in absorbance values at 220 nm and 275 nm, which is calculated utilizing the following equation: $\Delta A = A_{220\ nm} - A_{275\ nm}$. (c) The concentration of $NO_3^-$ and removal ratio of $NO_3^-$ in electrolyte solutions after different NITRR test durations of 0.5-Cu NCs/HL-COF at −0.6 V vs. RHE.

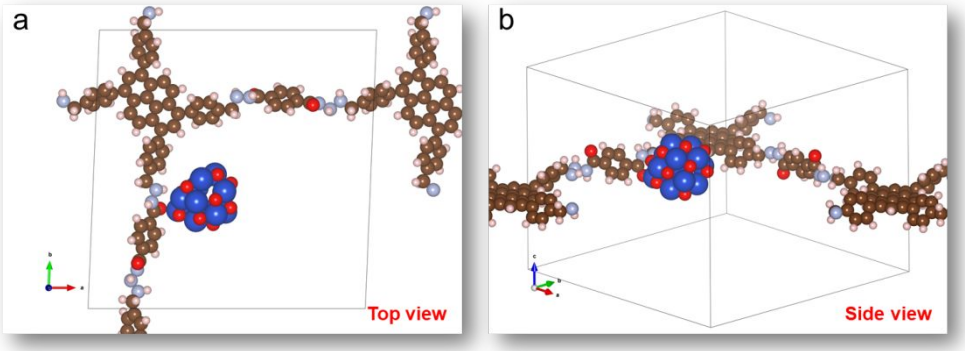


**Figure S18**. (a) Top view and (b) side view of the optimized Cu NCs/HL-COF structure.

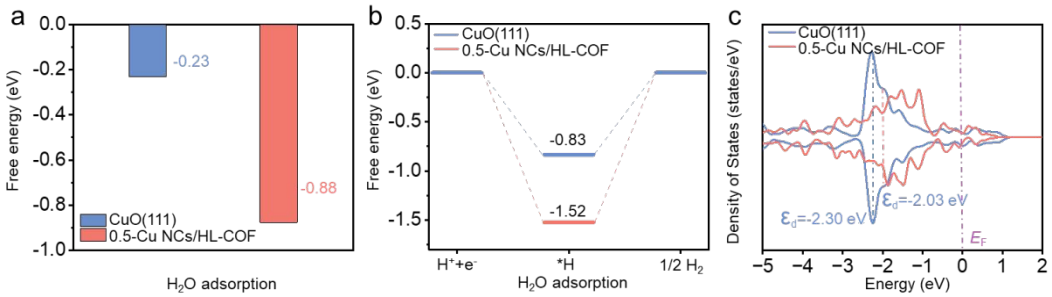


240

241 **Figure S19.** (a) $H_2O$ adsorption free energy, (b) hydrogen evolution reaction diagram,

242 and (c) PDOS of Cu 3*d* orbitals on CuO(111) and 0.5-Cu NCs/HL-COF, respectively.

243

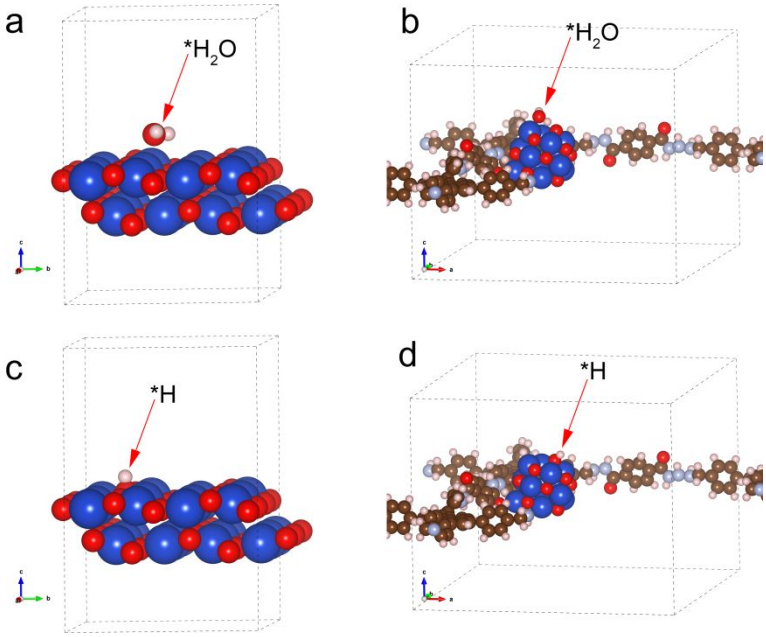


**Figure S20.** (a, b) *H and *$H_2O$ species on CuO(111). (c, d) *H and *$H_2O$ species on 0.5-Cu NCs/HL-COF.

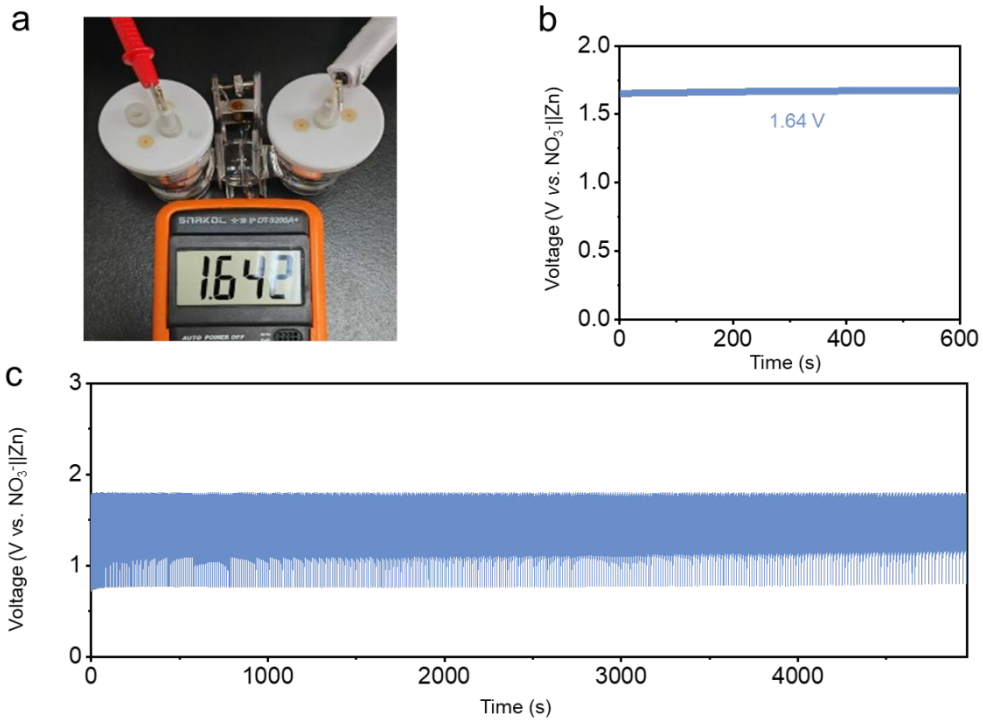


**Figure S21**. (a) Optical photograph of open-circuit potential (OCP) test curve of the NITRR||ZnOR battery. (b) OCP test curve of the NITRR||ZnOR battery assembled using the 0.5-Cu NCs/HL-COF cathode. (c) Charge-discharge cycling curves for the NITRR||ZnOR battery at 10 $mA \cdot cm^{-2}$ current density.

**Table S1.** EXAFS fitting parameters at the Cu K-edge for various samples.

| Sample | Path | *CN*[a] | *R*(Å)[b] | $\sigma^2$(Å$^2$)[c] | $\Delta E_0$(eV)[d] | *R* factor |
|---|---|---|---|---|---|---|
| **Cu foil** | Cu-Cu | 12.0* | 2.542±0.002 | 0.009±0.0005 | 4.4±0.6 | 0.004 |
| **$Cu_2O$** | Cu-O | 1.7±0.2 | 1.852±0.002 | 0.004±0.001 | 8.3±0.9 | 0.009 |
| | Cu-Cu | 12.0* | 3.021±0.001 | 0.023±0.001 | | |
| **CuO** | Cu-O | 4.0* | 1.950±0.002 | 0.004±0.001 | -1.8±1.5 | 0.006 |
| **CuPc** | Cu-N | 4.0* | 1.944±0.001 | 0.003±0.001 | 7.5±1.5 | 0.016 |
| | Cu-C | 3.2±1.1 | 2.941±0.001 | 0.003±0.003 | | |
| **0.2-Cu NCs/HL-COF** | Cu-N | 1* | 1.955±0.001 | 0.006±0.001 | -3.7±0.9 | 0.005 |
| | Cu-O | 3.5±0.3 | 1.946±0.001 | 0.006±0.001 | | |
| | Cu-C | 1* | 2.893±0.001 | 0.003±0.004 | | |
| **0.5-Cu NCs/HL-COF** | Cu-N | 1* | 1.995±0.001 | 0.006±0.002 | -3.0±1.2 | 0.011 |
| | Cu-O | 3.3±0.5 | 1.942±0.001 | 0.006±0.002 | | |
| | Cu-C | 1* | 2.962±0.001 | 0.002±0.003 | | |

[a] *CN*, coordination number; [b] *R*, the distance to the neighboring atom; [c] $\sigma^2$, the Mean Square Relative Displacement (MSRD); [d] $\Delta E_0$, inner potential correction; *R* factor indicates the goodness of the fit. $S_0^2$ was fixed to 1, according to the experimental EXAFS fit of Cu foil by fixing *CN* as the known crystallographic value. * This value was fixed during EXAFS fitting, based on the known structure of Cu. Fitting range: $3.0 \le k$ (/Å) $\le 12.0$ and $1.0 \le R$ (Å) $\le 3.0$ (Cu foil); $3.0 \le k$ (/Å) $\le 12.0$ and $1.0 \le R$ (Å) $\le 2.0$ (CuO); $3.0 \le k$ (/Å) $\le 12.0$ and $1.0 \le R$ (Å) $\le 3.0$ ($Cu_2O$); $3.0 \le k$ (/Å) $\le 11.0$ and $1.0 \le R$ (Å) $\le 2.9$ (CuPc); $3.0 \le k$ (/Å) $\le 12.0$ and $1.0 \le R$ (Å) $\le 3$ (0.2-Cu NCs/HL-COF); $3.0 \le k$ (/Å) $\le 12.0$ and $1.0 \le R$ (Å) $\le 3$ (0.5-Cu NCs/HL-COF). A reasonable range of EXAFS fitting parameters: $0.700 < S_0^2 < 1.000$; $CN > 0$; $\sigma^2 > 0$ Å$^2$; $|\Delta E_0| < 15$ eV; *R* factor < 0.02.

**Table S2.** The NITRR performance comparison of 0.5-Cu NCs/HL-COF with other representative electrocatalysts reported in previous literature.

| Ref. | Catalyst | $FE_{NH3}$ (%) | $NH_3$ yield | Potential (V vs RHE) | Electrolyte |
|---|---|---|---|---|---|
| **This work** | **0.5-Cu NCs/HL-COF** | **98.6** | **748.3 μmol·mg$^{-1}$·h$^{-1}$** | **−1.0** | **0.1 M $Na_2SO_4$ + 0.01 M $KNO_3$** |
| Ref. 1 | TpBpy-Cu-F | 82.6 | 2.7 mg·h$^{-1}$·cm$^{-2}$ | −0.746 | 0.5 M $Na_2SO_4$ + 0.1 M $NaNO_3$ |
| Ref. 5 | BECOF/PdCu | 91.0 | 11.01 mmol·h$^{-1}$·g$^{-1}_{cat}$ | −1.3 | 0.05 M $H_2SO_4$ + 0.1 M $KNO_3$ |
| Ref. 16 | NiTP-CoTAPP MCOF | 85.6 | 160.2 mmol·h$^{-1}$·g$^{-1}_{cat}$ | −0.8 | 0.1 M $Na_2SO_4$ + 0.5 M $KNO_3$ |
| Ref. 38 | Cu/$Cu_2O$@COF | 95 | 3.4 mmol·mg$^{-1}$·h$^{-1}$ | −0.8 | 1 M KOH + 0.1 M $KNO_3$ |
| Ref. 39 | Py-Bpy-Fe | 91.2 | 3.91 mmol·h$^{-1}$·g$^{-1}_{cat}$ | −1.845 | 1 M KOH + 0.1 M $KNO_3$ |
| Ref. 40 | PEPy-2CHO-TTA COF | 95 | 5.8 mg·h$^{-1}$·cm$^{-2}$ | −0.6 | 1 M KOH + 0.1 M $KNO_3$ |
| Ref. 41 | 2D-CuPc-COF | 95.4 | 24.6 mg·h$^{-1}$·cm$^{-2}$ | −1.4 | 0.5 M $K_2SO_4$ + 0.1M $KNO_3$ |
| Ref. 42 | Zn-TAPP-TTF | 71.4 | 542.3 μmol·h$^{-1}$·mg$^{-1}_{cat}$ | −1.4 | 0.1 M $KHCO_3$ + 0.1 M $KNO_2$ |
| Ref. 49 | NiPr-TPA-COF | 90.0 | 2.5 mg·h$^{-1}$·cm$^{-2}$ | −1.645 | 0.5 M $K_2SO_4$ + 0.3 M $KNO_3$ |
| Ref. 53 | COF-366-Fe | 85.4 | 1.88 mmol·h$^{-1}$·mg$^{-1}_{cat}$ | −1.945 | 0.5 M $K_2SO_4$ + 0.1M $KNO_3$ |
| Ref. 55 | HOF-Cu | 93.8 | 0.65 mmol·h$^{-1}$·cm$^{-2}$ | −1.0 | 0.5 M $K_2SO_4$ + 0.1M $KNO_3$ |

**Table S3**. Free energy (eV) correction for the NITRR intermediates on Cu

272 NCs/HL-COF.

273

| Intermediates | ZPE | TΔS |
|---|---|---|
| ***$NO_3$** | 0.42 | 0.23 |
| ***$HNO_3$** | 0.73 | 0.21 |
| ***$NO_2$** | 0.33 | 0.16 |
| ***$HNO_2$** | 0.59 | 0.16 |
| ***NO** | 0.16 | 0.10 |
| ***NHO** | 0.42 | 0.15 |
| ***NHOH** | 0.80 | 0.17 |
| ***$NH_2OH$** | 1.15 | 0.20 |
| ***$NH_2$** | 0.68 | 0.11 |

274

275

**Reference**

S1. G. Kresse , J. F., Efficiency of ab-initio total energy calculations for metals and semiconductors using a plane-wave basis set. *Comput. Mater. Sci.* **1996,** *6* (1), 15-50.

S2. Kresse, G.; Furthmüller, J., Efficient iterative schemes for ab initio total-energy calculations using a plane-wave basis set. *Phys. Rev. B* **1996,** *54* (16), 11169-11186.

S3. Kresse, G.; Hafner, J., Ab initio molecular-dynamics simulation of the liquid-metal-amorphous-semiconductor transition in germanium. *Phys. Rev. B* **1994,** *49* (20), 14251-14269.

S4. Perdew, J. P.; Chevary, J. A.; Vosko, S. H.; Jackson, K. A.; Pederson, M. R.; Singh, D. J.; Fiolhais, C., Atoms, molecules, solids, and surfaces: Applications of the generalized gradient approximation for exchange and correlation. *Phys. Rev. B* **1992,** *46* (11), 6671-6687.

S5. Blöchl, P. E., Projector augmented-wave method. *Phys. Rev. B* **1994,** *50* (24), 17953-17979.

S6. Monkhorst, H. J.; Pack, J. D., Special points for brillouin-zone integrations. *Phys. Rev. B* **1976,** *13* (12), 5188-5192.

S7. Li, L.; Zhang, R.; Vinson, J.; Shirley, E. L.; Greeley, J. P.; Guest, J. R.; Chan, M. K. Y., Imaging catalytic activation of $CO_2$ on $Cu_2O$ (110): A first-principles study. *Chem. Mater.* **2018,** *30* (6), 1912-1923.